ACS APPLIED MATERIALS & INTERFACES

Research Article

www.acsami.org

Tunable Ultraviolet Photoresponse in Solution-Processed p−n Junction Photodiodes Based on Transition-Metal Oxides

Ting Xie,[†,‡,⊥] Guannan Liu,[†,‡,§,⊥] Baomei Wen,[†] Jong Y. Ha,[†,§] Nhan V. Nguyen,[∥] Abhishek Motayed,[†,§] and Ratan Debnath*[,†]

[†]Materials Science and Engineering Division, Material Measurement Laboratory, National Institute of Standards and Technology, Gaithersburg, Maryland 20899, United States

[‡]Department of Electrical and Computer Engineering, University of Maryland, College Park, Maryland 20742, United States

[§]Institute for Research in Electronics and Applied Physics, University of Maryland, College Park, Maryland 20742, United States

[∥]Semiconductor and Dimensional Metrology Division, Physical Measurement Laboratory, National Institute of Standards and Technology, Gaithersburg, Maryland 20899, United States

Supporting Information

ABSTRACT: Solution-processed p−n heterojunction photodiodes have been fabricated based on transition-metal oxides in which NiO and ternary $Zn_{1-x}Mg_xO$ (x = 0−0.1) have been employed as p-type and n-type semiconductors, respectively. Composition-related structural, electrical, and optical properties are also investigated for all the films. It has been observed that the bandgap of $Zn_{1-x}Mg_xO$ films can be tuned between 3.24 and 3.49 eV by increasing Mg content. The fabricated highly visible-blind p−n junction photodiodes show an excellent rectification ratio along with good photoresponse and quantum efficiency under ultraviolet (UV) illumination. With an applied reverse bias of 1 V and depending on the value of x, the maximum responsivity of the devices varies between 0.22 and 0.4 A/W and the detectivity varies between 0.17×10^{12} and 2.2×10^{12} cm $(Hz)^{1/2}/W$. The photodetectors show an excellent UV-to-visible rejection ratio. Compositional nonuniformity has been observed locally in the alloyed films with x = 0.1, which is manifested in photoresponse and X-ray analysis data. This paper demonstrates simple solution-processed, low cost, band tunable photodiodes with excellent figures of merit operated under low bias.

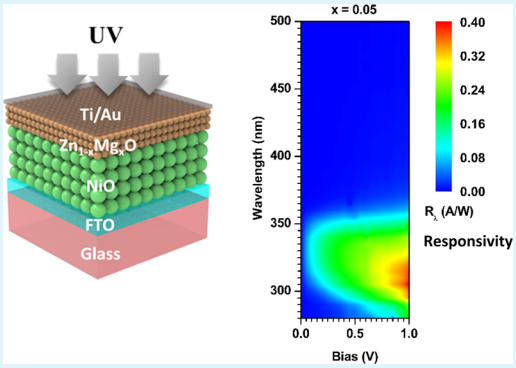

KEYWORDS: *photodetector, NiO, $Zn_{1-x}Mg_xO$, TMO*

INTRODUCTION

Transition-metal oxides (TMOs) have attracted considerable attention in recent years within the research community because of their versatile applications in transparent thin-film transistors,[1,2] ultraviolet light-emitting diodes,[3,4] transparent electrodes,[5] and ultraviolet (UV) photodetectors (PD).[6−9] The applications of these oxides mainly rely on their intrinsic properties, including optical transparency in the near-UV and visible spectra, low impact on the environment, and thermal stability, as well as heterojunctions composed of different types of TMOs, or specifically p−n junctions.[7] Among various demonstrated TMO materials utilized in p−n heterojunction UV PDs, NiO and ZnO, which are p- and n-type semiconductors, respectively, are particularly favored because of their distinguished electrical and optical properties.[3,7,10−12] Benefiting from a direct band gap of 3.3 eV and an exciton binding energy of 60 meV, the II−VI semiconductor ZnO has been employed for applications in optoelectronic devices.[13] Moreover, the band gap can be engineered between 3.3 eV (ZnO) and 7.8 eV (MgO) by formation of $Zn_{1-x}Mg_xO$ (ZMO) alloys.[14,15] The alloyed ZMO maintains high optical transparency to visible wavelengths, which is indispensable for transparent optoelectronic applications.[12] Additionally, low dislocation density during heteroepitaxy,[16] high-energy radiation resistance,[17] and chemical stability[18] distinguish ZnO (and ZMO) from other wide band gap semiconductors such as GaN (and its alloy $Al_xGa_{1-x}N$), ZnSe, and SiC.

For UV PD applications, ZMO has been primarily realized either as a photoconductor[19] or a Schottky photodiode.[20,21] In most of the cases, ZMO films have been prepared via prohibitively expensive and sophisticated deposition techniques, such as pulsed laser deposition (PLD),[15,22] sputtering,[15,23] chemical vapor deposition (CVD),[24] and molecular beam epitaxy (MBE),[25,26] and they all require energy intensive, high vacuum deposition processes. However, metal−semiconductor−metal (MSM) and Schottky barrier PDs have their own advantages, such as simple planar structure, no UV absorption by metal contact as well as low stray capacitance for

Received: February 13, 2015
Accepted: April 21, 2015
Published: April 21, 2015

DOI: 10.1021/acsami.5b01420
ACS Appl. Mater. Interfaces 2015, 7, 9660−9667

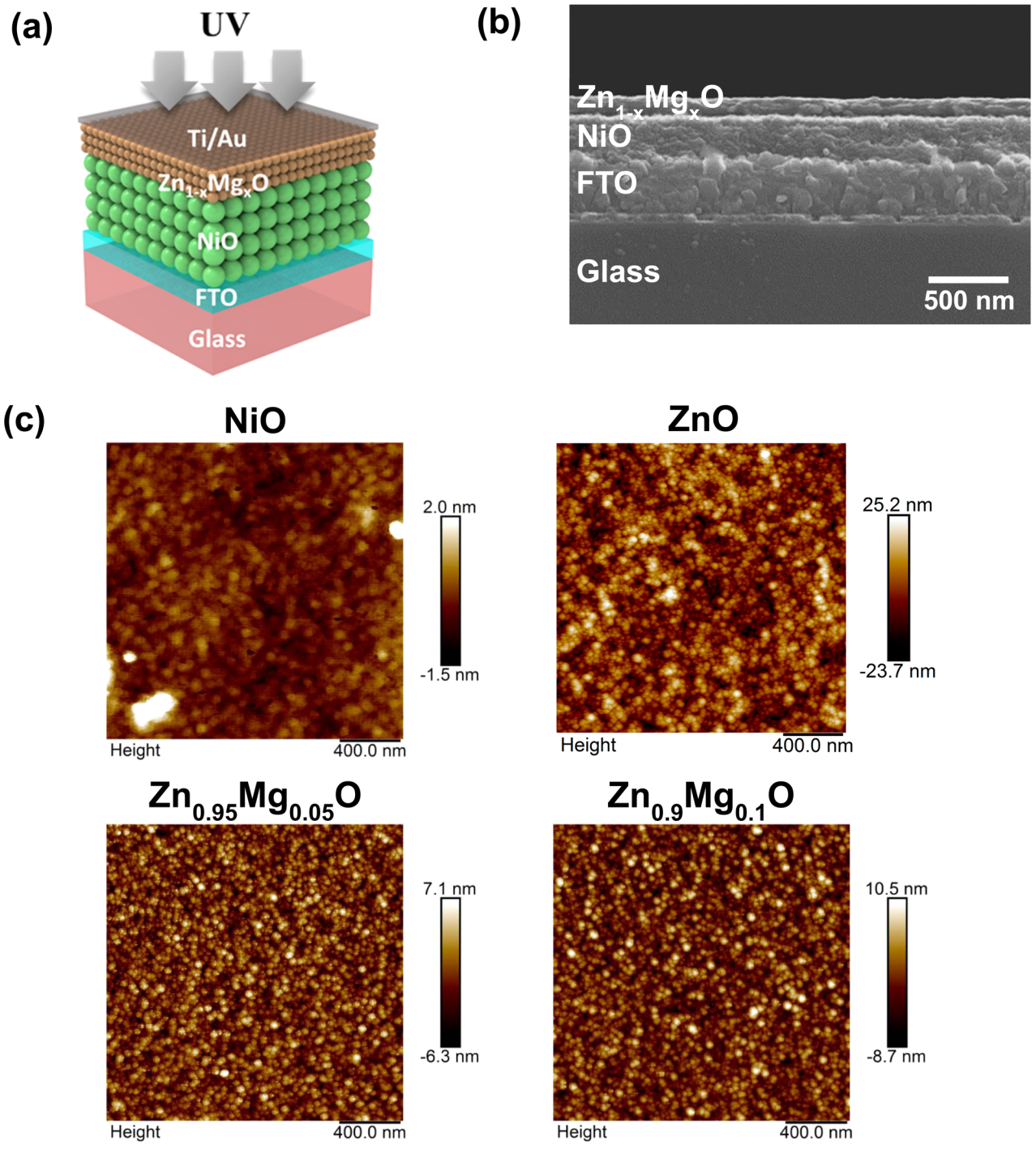

Figure 1. NiO/$Zn_{1-x}Mg_xO$ heterojunction PD: (a) Schematic of the device showing metal oxides along with FTO and Ti/Au metal contacts; (b) cross-sectional SEM image of an actual device with $x = 0.05$; and (c) AFM images of all the TMOs spin coated on silicon substrates after annealing them at 450 °C for 20 min in air. The nanograins are evident from the AFM images.

the former and fabrication simplicity, high speed and absence of high-temperature diffusion processes for the later, p−n junction detectors have even more advantags, viz., low or zero bias currents, high impedance, built in voltage larger than that of a Schottky diode made with the same semiconductor, as well as low saturation current. In contrast to the well-illustrated performance of p-NiO/n-ZnO heterojunctions for UV PD applications,[7,8,27] there have been few reports on homojunction $Zn_{1-x}Mg_xO$,[28,29] but p−n heterojunctions made with other non-Zn-based oxides are lacking using sol−gel method.

In this work, we have successfully fabricated TMO UV PDs comprising solution-processed p-NiO and n-$Zn_{1-x}Mg_xO$ (x = 0−0.1) layers on conductive fluorine-doped tin oxide (FTO) covered glass substrates. Sol−gel $Zn_{1-x}Mg_xO$ thin films show a hexagonal wurtzite type of crystalline structure and no significant change of grain morphology for all the films studied. The devices show prominent but tunable UV photoresponse with various Mg contents consistent with the bandgap of alloyed ZnO. For higher Mg content (x = 0.1), compositional

DOI: 10.1021/acsami.5b01420
ACS Appl. Mater. Interfaces 2015, 7, 9660−9667

nonuniformity has been observed over the film which is manifested in the device's optical properties.

EXPERIMENTAL DETAILS

Precursor Solution. For NiO, nickel acetate tetrahydrate was dissolved in 2-methoxyethanol and monoethanolamine (MEA) in a glass vial. Similarly, $Zn_{1-x}Mg_xO$ precursor solution was prepared separately using zinc acetate tetrahydrate and magnesium acetate tetrahydrate in the same solvents. The molar ratio of Ni^{2+}:MEA or (Zn^{2+} + Mg^{2+}):MEA was maintained at 1:1 in the solution. The concentration of Mg^{2+} was adjusted to form $Zn_{1-x}Mg_xO$ thin films with x ranging from 0 to 0.1. Concentration of all metal ions was 0.4 M. The dissolved precursors were magnetically stirred at 60 °C for 2 h in a water bath and then filtered with a 0.45 μm filter.

Device Fabrication. The FTO/glass substrates were cleaned with acetone and isopropanol in an ultrasonic bath, rinsed with deionized water, and finally dried with N_2 gas. For thin-film fabrication, NiO precursor was spin-coated on the substrates and the film was immediately dried at 300 °C for several minutes on a preheated hot plate in a fumehood. The procedure was repeated multiple times to achieve film thickness of 250 to 300 nm. The same procedure was repeated for $Zn_{1-x}Mg_xO$ to obtain ≈90−120 nm thick film. Finally, the films were annealed at 400 °C for 20 min in air. Ultrathin Ti (10 nm)/Au (3 nm) top contacts were deposited by electron-beam evaporation at a rate of about (0.5−1) Å/s through a metal mask having an array of circular openings of 3.8 mm. No process optimization was performed.

Characterization Methods. Surface morphology and cross-sectional structure of the PDs were examined using a Bruker Dimension FastScan atomic force microscopy (AFM) instrument and a Hitachi-4700 high-resolution scanning electron microscopy (SEM) instrument equipped with energy dispersive X-ray spectrometry (EDS). [Certain commercial equipment, instruments, or materials are identified in this paper in order to specify the experimental procedure adequately. Such identification is not intended to imply recommendation or endorsement by the National Institute of Standards and Technology, nor is it intended to imply that the materials or equipment identified are necessarily the best available for the purpose.] Cross-sectional images were taken from freshly cleaved samples after coating them with carbon to avoid charging effects. Structural characterization of the oxide films was conducted using conventional X-ray diffraction (XRD). Vacuum ultraviolet variable angle ellipsometry (VUV-VASE) measurements were performed to determine the dielectric functions of the films from which optical band gaps were extracted by employing Tauc plots.[30]

Devices were characterized for current−voltage (I−V) and external quantum efficiency (EQE) using a spectrally filtered light source. Because of the device structure, it was not possible to illuminate through the glass side. Also, FTO absorbs most of the UV light below 320 nm as compared to ultrathin Ti/Au. Hence, the devices were illuminated through metal contacts during the measurement. EQE system was calibrated using a NIST-calibrated silicon photodiode, and a total uncertainty of ±5% (fractional) is associated with measured EQE.

RESULTS AND DISCUSSION

Figure 1a shows the schematic of the PD with various components associated with the p−n junction photodiode. A cross-sectional SEM image of a representative device as well as the top-view AFM images of the annealed NiO and $Zn_{1-x}Mg_xO$ thin films are also depicted in panels b and c of Figure 1, respectively. The SEM image clearly shows the multilayer structure of the PD for nominal Mg concentration of x = 0.05, showing various oxide layers on FTO/glass substrates. The thicknesses of spin-coated NiO and $Zn_{0.95}Mg_{0.05}O$ have been estimated to be about 250 and 120 nm, respectively. The sharp interface between NiO and $Zn_{0.95}Mg_{0.05}O$ indicates smooth

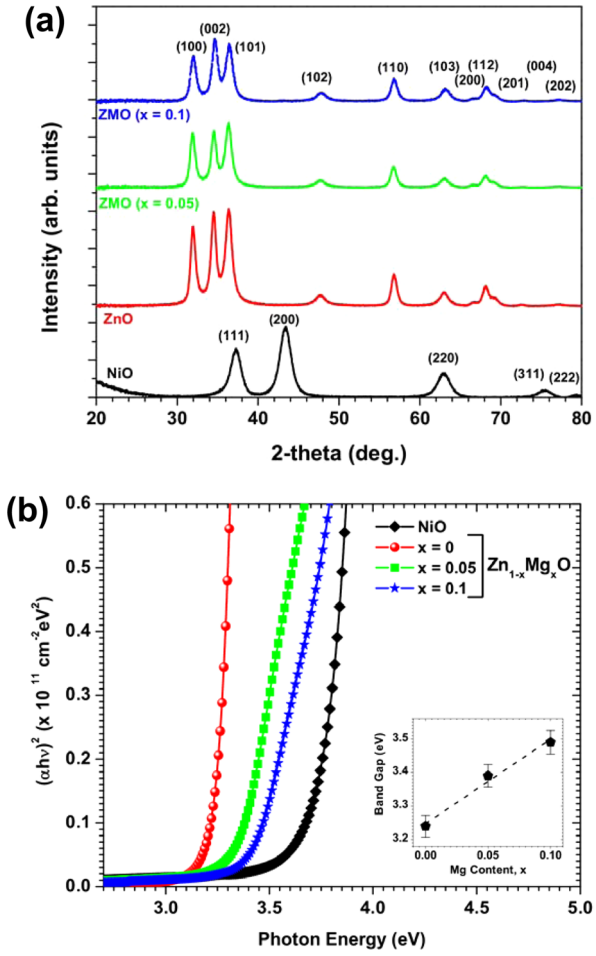

Figure 2. (a) XRD scans showing diffraction peaks coming from cubic and hexagonal structures of NiO and $Zn_{1-x}Mg_xO$, respectively. XRD measurements confirm the formation of metal oxides as well as no MgO phase for the alloyed sample. (b) Estimation of the direct energy band gap of all the oxides from ellipsometry measurements (Tauc plot). The inset shows the linear fit of the measured band gap as a function of Mg content.

surfaces of fabricated films, which is further verified by AFM results shown in Figure 1c, whereas nonuniform interface between FTO and NiO is observed. Lifetime of photogenerated carrier is a crucial factor in determining the performance of a PD. The photogenerated minority carrier outside the depletion region (the interface) has a very short lifetime because of fast recombination with majority carriers. Hence, the effective region of a UV PD is the depletion region, i.e., the interface. Meanwhile, defects in the interface will greatly reduce the lifetime of photogenerated charge carriers in terms of enhanced possibility of scattering and functioning as recombination centers. Therefore, a sharp, high-quality interface ensures better performance of the PD.

High-resolution AFM images reveal polycrystalline nanoscale grains and smooth surfaces of the spin-coated, annealed films. The grain size of $Zn_{1-x}Mg_xO$ (x = 0.05, 0.1) film is comparable to ZnO film with typical diameter ranged between 20 to 25 nm. The resemblance in granularity of $Zn_{1-x}Mg_xO$ and ZnO films originates from the similarity of the ionic radii of Zn^{2+} and Mg^{2+}.[31] However, $Zn_{1-x}Mg_xO$ (x = 0.05, 0.1) films exhibit much smoother surfaces when compared to ZnO film. The calculated root-mean-square (rms) roughness for $Zn_{1-x}Mg_xO$

DOI: 10.1021/acsami.5b01420
ACS Appl. Mater. Interfaces 2015, 7, 9660−9667

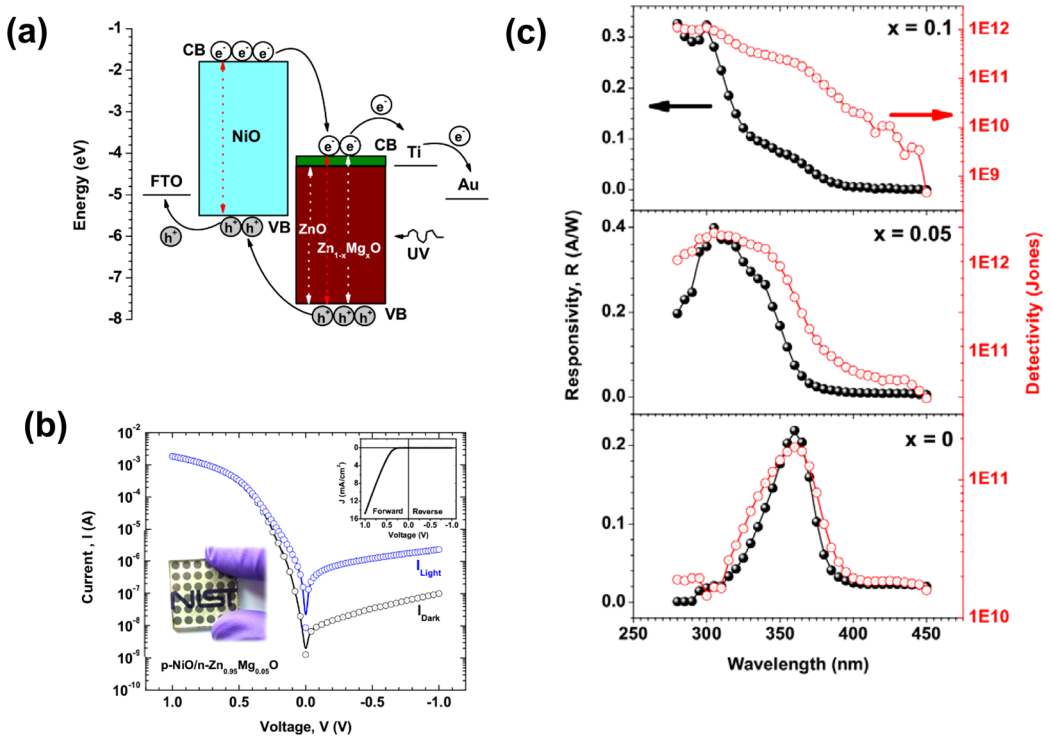

Figure 3. (a) Energy levels of various components in the PDs. The conduction band (CB) of $Zn_{1-x}Mg_xO$ changes with Mg content whereas valence band (VB) position remains the same. Photogenerated electrons and holes move to their respective contact. (b) Current−voltage (I−V) plot of the p-NiO/n-$Zn_{0.95}Mg_{0.05}O$ heterojunction diode in dark and UV illumination at 335 nm with 1.2 μW power. The positive voltage stands for forward bias, and the negative values mean reverse bias. The rectifying nature of the diode (see the inset linear current-density, J, and voltage, V, plot of the diode in the dark at forward and reverse bias) as well as the photoresponse are evident from the I−V data. Another inset shows the actual PD with NIST logo underneath. (c) Responsivity and detectivity of all the devices at 1 V reverse bias.

(x = 0, 0.05, 0.1) are 7.15, 2.02, and 2.63 nm, respectively. In contrast, NiO film shows relatively larger gain size, roughly 40 nm, with a much diminished rms value of 0.45 nm. The low surface roughness and small granularity of engineered NiO and $Zn_{1-x}Mg_xO$ films make them suitable for applications in abrupt heterojunctions.

Figure 2a shows XRD patterns of prepared NiO and $Zn_{1-x}Mg_xO$ (x = 0, 0.05, 0.1) films. All the diffraction peaks can be identified as cubic NiO (JCPDS entry 78-0643) or hexagonal wurtzite ZnO structure (JCPDS entry 36-1451), accordingly. These results imply that the fabricated ZMO films retain the ZnO hexagonal wurtzite crystal structure without any segregation of MgO phase. The broad diffraction peaks are in agreement with the polycrystalline nature and the small grain size of processed thin films. A subtle shifting of ZnO(002) toward higher diffraction angle from 34.51° (x = 0) to 34.68° (x = 0.1) with an increase in Mg content is identified in Figure 2a. This observation can be attributed to the slightly lower ionic radii of Mg^{2+}, which decreases the grain size of ZMO in the c-axis.

To understand the optical absorption and bandgap energy of NiO and $Zn_{1-x}Mg_xO$, absorption coefficients (α) are calculated from the pseudodielectric functions of the thin films using ellipsometry. The optical band gap (E_g) is then derived from the Tauc plot, which is a linear relationship of $(\alpha h\nu)^2$ versus $h\nu$ where $h\nu$ is the photon energy (Figure 2b). E_g is deduced from a linear fit to the near band gap spectral region and is found to be ≈3.72 eV for NiO, which is an agreement with reported data.[9] For $Zn_{1-x}Mg_xO$ films, there is a gradual blue shift of the fundamental absorption edges with the increase of Mg concentration. The value increases linearly from 3.24 eV for x = 0 to 3.49 eV for x =0.1, which can be fitted with the equation $E_g = (3.248 + 2.51x)$ eV. It must be noted here that for x = 0.1, the Tauc plot shows another linear regime at lower energy (below 3.7 eV) in addition to the one used for linear fitting, and this may indicate some composition variation across the sample as will be shown later. Although the ionic radius of Mg^{2+} ions (0.57 Å) is almost equal to that of Zn^{2+} ions (0.60 Å),[31] which might imply a wide range of solubility of Mg in ZnO, the thermodynamic solubility limit of Mg in ZnO is a mole fraction of only 4%.[32] However, solid solubility of MgO in ZnO has been reported to be mole fraction of 33% for thin films deposited by PLD[15] and 43% deposited by MBE.[33] The sol−gel method is based on equilibrium growth conditions; thus, the solubility is influenced by the starting precursors, solvents, temperature, etc. as opposed to other nonequilibrium growths. The compositional fluctuations in solution-processed $Zn_{1-x}Mg_xO$ systems have also been reported for modest[34,35] to higher[36] Mg content, and our data also indicate some possible compositional variation for x = 0.1. The estimated bandgap values are also consistent with the EQE measurements (see Supporting Information, Figure S1). In any case, all the films are highly transparent in the visible range, which makes them suitable for UV PDs. Considering the limitation of this sol−gel technique, one can utilize either PLD- or MBE-grown $Zn_{1-x}Mg_xO$ on NiO to avoid such compositional nonuniformity at higher Mg content.

The energy levels of various components of the PD are shown in Figure 3a, where $Zn_{1-x}Mg_xO$ is depicted as a tunable bandgap system because of different Mg content. On the basis of the reported data, incorporation of Mg^{2+} into ZnO leads to the modifications of conduction band (CB) edge of the ternary

DOI: 10.1021/acsami.5b01420
ACS Appl. Mater. Interfaces 2015, 7, 9660−9667

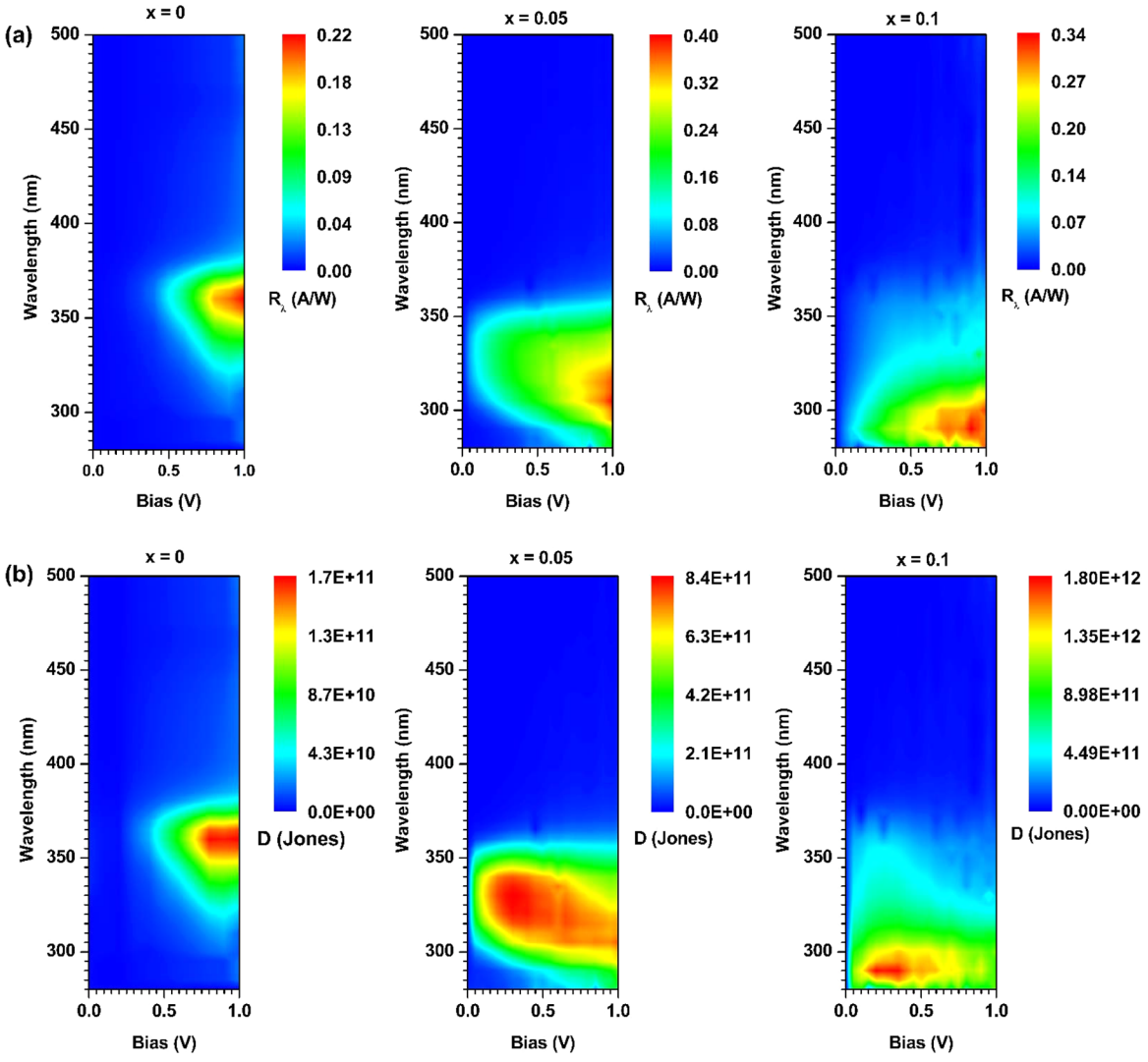

Figure 4. Device performance of NiO/$Zn_{1-x}Mg_xO$ heterojunctions with various Mg content, x, as a function of applied reverse bias: (a) responsivity, R_λ, and (b) detectivity, D.

oxide whereas the valence band (VB) edge remains unchanged.[37] Thus, the CB edge changes within ≈0.25 eV as the corresponding bandgap of $Zn_{1-x}Mg_xO$ varies from 3.24 to 3.49 eV with an increase in Mg content (x = 0−0.1). Under UV illumination, the photogenerated electrons are transported through the $Zn_{1-x}Mg_xO$ layer to the Ti/Au cathode and the holes are transported from the NiO to the FTO anode. On the basis of the band-edge energy offsets, NiO/$Zn_{1-x}Mg_xO$ layers form a type-II heterojunction (Figure 3a). The built-in field as well as the energy gradient at the type-II interface enables spatial separation of electrons and holes. The current−voltage characteristics of the heterojunction diodes reveal the anticipated rectifying behavior in the dark and exhibit an excellent rectification ratio of ≈18 500 at ±1 V (inset of Figure 3b). Under UV illumination, current enhancement is observed under forward and reverse bias because of the photogenerated carriers. It is worthwhile to mention here that the current density of the devices decreases after Mg alloying because of the increase in resistivity. Undoped ZnO is an n-type material, and the higher carrier density is attributed to the interstitial zinc and/or oxygen vacancy.[38] When Mg is incorporated into ZnO, the oxygen vacancies are suppressed, which reduces the carrier density in the film.[39] Hence, dark current decreases from 100 to 18 nA at a reverse bias of 1 V when the Mg content increases from 0.05 to 0.1. The ideality factor of the diode also increases (see Supporting Information, Table S1).

The spectral response of the PD is obtained by scaling the measured photocurrent with that of a calibrated Si photodetector, given nominally identical illumination under applied reverse bias. The responsivity (R_λ) and the specific detectivity (D^*), which are the figures of merit of the PD, have been calculated using the following equations:[40]

$$R_\lambda = \frac{I_{light}}{P_0}$$

$$D^* = \frac{R_\lambda}{\sqrt{2qJ_{dark}}}$$

where I_{light} is the photocurrent of the device under UV illumination, P_0 the light intensity, and J_{dark} the dark current at the same value of reverse bias used for R_λ. It has been assumed that the dark current is the major source of shot noise. Typical responsivity and detectivity of NiO/$Zn_{1-x}Mg_xO$ devices under a reverse bias of 1 V are shown in Figure 3c for the spectral range 280 to 450 nm. For ZnO (x = 0), the peak response

DOI: 10.1021/acsami.5b01420
ACS Appl. Mater. Interfaces 2015, 7, 9660−9667

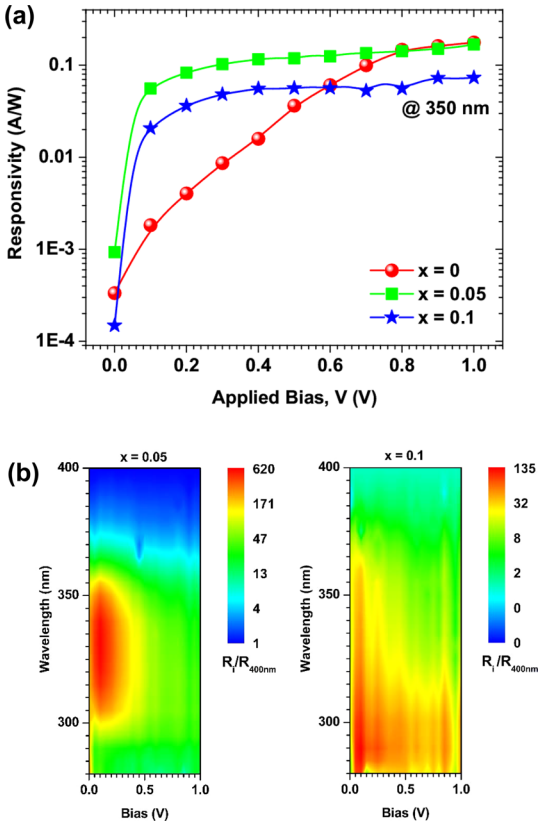

Figure 5. (a) NiO/$Zn_{1-x}Mg_xO$ heterojunction device response at 350 nm as a function of applied bias. (b) UV−visible rejection ratio (R_i/$R_{400\ nm}$) for Mg content of x = 0.05 and 0.1 in which i = (280−400) nm.

occurs at 360 nm with the responsivity of 0.22 A/W. The −3 dB cutoff edge is close to the absorption edge of ZnO. The photoresponse maxima are blue-shifted for $Zn_{1-x}Mg_xO$ alloy films, consistent with the increase of bandgap. For $Zn_{0.95}Mg_{0.05}O$, the maximum responsivity reaches to 0.4 A/W at 310 nm and there is no discernible responsivity for photons below 360 nm. In the case of $Zn_{0.9}Mg_{0.1}O$, the responsivity peaks at 300 nm followed by a sharp decrease at 340 nm, which is close to the bandgap of NiO, and then slower decrease above 350 nm, which corresponds to the absorption edge of $Zn_{0.9}Mg_{0.1}O$. The responsivity goes further beyond the band gap of $Zn_{0.9}Mg_{0.1}O$, indicating a possible composition fluctuation across the sample. To verify this, EDS analysis has been performed for the compositional analyses of Mg and Zn in all the samples. The values are plotted as a function of nominal Mg content (x) and compared with the measured Mg:Zn values (see Supporting Information, Figure S2). The experimental Mg:Zn ratio shows less deviation from its nominal value for Mg content of x = 0.05, whereas it deviates significantly for x = 0.1. Hence, these data suggest a local compositional nonuniformity for higher Mg content which is beyond the thermodynamic solubility limit. Furthermore, it is possible that Mg may incorporate into NiO during annealing, and this is likely to increase the bandgap of NiO;[41] hence, the photoresponse of the alloyed samples further extends to the shorter wavelength. In contrast, the ionic radius of Ni^{2+} ions (0.55 Å) is also similar to that of Zn^{2+} (0.60 Å).[31] Thus, there can be Zn^{2+} diffusion into NiO although one may expect a different level of Zn^{2+} incorporation into NiO as compared to Mg^{2+} because of its relatively larger size. Investigating these effects is beyond the scope of this paper. Detectivity, which characterizes the normalized signal-to-noise performance of a PD, is another figure of merit, and the measured data show the maximum detectivity of (0.17−2.2) × 10^{12} cm $(Hz)^{1/2}$/W or Jones depending on the composition. Overall, the data clearly show that one can tune the response of the heterojunction NiO/$Zn_{1-x}Mg_xO$ system simply by tuning the ZMO bandgap.

The advantages of operating a photodiode under zero or low bias voltage are the low dark current, low noise level, and large dynamic range. Thus, the device performance was further assessed below 1 V reverse bias, as shown in Figure 4. When the devices were tested in the photovoltaic mode (i.e., under zero bias), the flow of photocurrent out of the device is restricted. Hence, the responsivity is very low, particularly for NiO/ZnO devices (maximum value is 0.34 mA/W at 340 nm). For x = 0.05, it is 1.4 mA/W; the detectivity is ~6.76 × 10^{10} Jones, both at 340 nm. When the bias is increased across the device, there is no appreciable response from the NiO/ZnO device below 0.5 V (Figure 5a). However, for the alloyed samples, the strong response is detected under the same bias. ZnO is intrinsically an n-type semiconductor with high carrier concentration and thus at equilibrium, resulting in smaller depletion widths[42] and lower quantum yields because the minority carrier (i.e., holes for ZnO) diffusion lengths are very short in these materials.[43] Upon illumination, the minority carrier current increases, mostly from electron−hole pairs generated within the depletion region. The collection efficiency is very inefficient in the quasi-neutral region (part of the device beyond the depletion region) because of the small minority carrier diffusion length; thus, recombination can take place. For Mg alloyed devices, the resistivity goes up, which is analogous

Table 1. Performance Matrix of Various $Zn_{1-x}Mg_xO$-Based PDs Reported in the Literature

material system	configuration	growth method	bias (V)	max. R_λ (A/W)	max. D^* (Jones)	ref
$Zn_{0.38}Mg_{0.62}O$	MSM	MBE	10	1.664	–	44
$Zn_{0.5}Mg_{0.5}O$	p−n	MBE	2	6*m*	–	45
$Zn_{0.53}Mg_{0.47}O$	MSM	sputtering	5	10.6*m*	–	46
$Zn_{0.66}Mg_{0.34}O$	MSM	PLD	10	0.8	–	29
$Zn_{0.66}Mg_{0.34}O$	MSM	PLD	5	1200	–	19
$Zn_{0.76}Mg_{0.24}O$	p−n	MBE	9	0.4*m*	1.8 × 10^{10}	28
$Zn_{0.8}Mg_{0.2}O$	MSM	sputtering	3	0.02	3.1 × 10^{11}	47
$Zn_{0.82}Mg_{0.18}O$	Schottky	CVD	1.5	32	–	48
NiO−ZnO	p−n	sol−gel	1	0.28	6.3 × 10^{11}	27
NiO−ZnO	p−n	sol−gel	1	10.2	1 × 10^{12}	49
NiO−$Zn_{1-x}Mg_xO$	**p−n**	**sol−gel**	**1**	**0.22−0.4**	**(0.17−2.2) × 10^{12}**	**this work**

DOI: 10.1021/acsami.5b01420
ACS Appl. Mater. Interfaces 2015, 7, 9660−9667

to the enhancement in bandgap, and the free carrier density decreases. Thus, the depletion width on $Zn_{1-x}Mg_xO$ side increases. Hence, NiO/$Zn_{1-x}Mg_xO$ (x = 0.05, 0.1) heterostructure diode shows a better photoresponse as compared to ZnO at the same low bias as the minority carriers in the sample are swept out by the large electric field despite having short diffusion length. The responsivity of the devices almost saturates at high bias, indicating carrier mobility saturation or sweep-out effect yielding a saturation of the current. The heterojunction devices also exhibit good UV-selective sensitivity with an excellent UV-to-visible rejection ratio.

The solar blindness is usually quantified in terms of rejection ratio, which is defined as the ratio of the photoresponse of a PD in the UV light to the visible light. A high UV-to-visible ratio is always desirable for the detector which will show very weak response to the solar visible spectrum and no filter is needed for UV detection. The rejection ratio for each wavelength was calculated from the responsivity at ith wavelength in the UV regime divided by the responsivity at 400 nm, (R_i/R_{400nm}, i = 280−400 nm). The maximum rejection ratio of over 600 has been achieved for $Zn_{1-x}Mg_xO$ with x = 0.05, and over 100 for x = 0.1 (Figure 5b). For x = 0.1, the responsivity of the device shows some (periodic) trend with no sharp cutoff under the applied bias because of the compositional fluctuation, and the same trend has also been seen in the rejection ratio. Finally, the performance of PDs in this work and some previously reported data are summarized in Table 1 for comparison. Considering the simplicity of such solution-processed p−n heterojunction architecture, the devices here show excellent figures of merit as compared to other oxide-based PDs.

CONCLUSIONS

Simple, cost-effective solution-processed p−n heterojunction UV photodetectors have been conveniently fabricated on FTO/glass substrates by spin-coating methods using wide-band gap NiO and $Zn_{1-x}Mg_xO$. Sol−gel $Zn_{1-x}Mg_xO$ thin films have hexagonal wurtzite type crystalline structure and nanograin morphology without any MgO phase. The fabricated heterojunction photodiode exhibits very low dark current under reverse bias with excellent rectification. The PDs have shown tunable photoresponse with superior responsivity and detectivity in the UV regime. Compositional nonuniformity has also been observed for high Mg content. Considering the advantages of solution-processable fabrication, the devices have potential for use in low cost, large-area UV PD applications.

ASSOCIATED CONTENT

Supporting Information

(a) Calculated bandgap of $Zn_{1-x}Mg_xO$ from EQE data at various Mg content, x; (b) extracted diode characteristics of the fabricated heterojunction devices; and (c) estimated Mg:Zn ratio in $Zn_{1-x}Mg_xO$ (x = 0.05, 0.1) using energy dispersive X-ray analysis. The Supporting Information is available free of charge on the ACS Publications website at DOI: 10.1021/acsami.5b01420.

AUTHOR INFORMATION

Corresponding Author

*E-mail: ratan.debnath@nist.gov.

Author Contributions

⊥T.X. and G.L.: These authors have made equal contributions to this paper.

Notes

The authors declare no competing financial interest.

ACKNOWLEDGMENTS

R.D. and J.Y.H. acknowledge the financial support of NIST Contract SB1341-13-SE-0216. The PD devices were fabricated in the Nanofab of the NIST Center for Nanoscale Science and Technology.

REFERENCES

(1) Nomura, K.; Ohta, H.; Takagi, A.; Kamiya, T.; Hirano, M.; Hosono, H. Room-Temperature Fabrication of Transparent Flexible Thin-Film Transistors Using Amorphous Oxide Semiconductors. *Nature* **2004**, *432*, 488−492.

(2) Nomura, K.; Ohta, H.; Ueda, K.; Kamiya, T.; Hirano, M.; Hosono, H. Thin-Film Transistor Fabricated in Single-Crystalline Transparent Oxide Semiconductor. *Science* **2003**, *300*, 1269−1272.

(3) Xi, Y. Y.; Hsu, Y. F.; Djurisic, A. B.; Ng, A. M. C.; Chan, W. K.; Tam, H. L.; Cheah, K. W. NiO/ZnO Light Emitting Diodes by Solution-Based Growth. *Appl. Phys. Lett.* **2008**, *92*, 113505.

(4) Ohta, H.; Kawamura, K.; Orita, M.; Hirano, M.; Sarukura, N.; Hosono, H. Current Injection Emission from a Transparent p-n Junction Composed of p-$SrCu_2O_2$/n-ZnO. *Appl. Phys. Lett.* **2000**, *77*, 475−477.

(5) Minami, T. Transparent Conducting Oxide Semiconductors for Transparent Electrodes. *Semicond. Sci. Technol.* **2005**, *20*, S35−S44.

(6) Ok, Y. H.; Lee, K. R.; Jung, B. O.; Kwon, Y. H.; Cho, H. K. All Oxide Ultraviolet Photodetectors Based on a p-Cu_2O Film/n-ZnO Heterostructure Nanowires. *Thin Solid Films* **2014**, *570*, 282−287.

(7) Ohta, H.; Hirano, M.; Nakahara, K.; Maruta, H.; Tanabe, T.; Kamiya, M.; Kamiya, T.; Hosono, H. Fabrication and Photoresponse of a p-n Heterojunction Diode Composed of Transparent Oxide Semiconductors, p-NiO and n-ZnO. *Appl. Phys. Lett.* **2003**, *83*, 1029−1031.

(8) Vygranenko, Y.; Wang, K.; Nathan, A. Low Leakage p-NiO/i-ZnO/n-ITO Heterostructure Ultraviolet Sensor. *Appl. Phys. Lett.* **2006**, *89*, 172105.

(9) Ohta, H.; Hirano, M.; Nakahara, K.; Maruta, H.; Tanabe, T.; Kamiya, M.; Kamiya, T.; Hosono, H. Fabrication and Photoresponse of a p-n Heterojunction Diode Composed of Transparent Oxide Semiconductors, p-NiO and n-ZnO. *Appl. Phys. Lett.* **2003**, *83*, 1029−1031.

(10) Kim, D. Y.; Ryu, J.; Manders, J.; Lee, J.; So, F. Air-Stable, Solution-Processed Oxide p−n Heterojunction Ultraviolet Photodetector. *ACS Appl. Mater. Interfaces* **2014**, *6*, 1370−1374.

(11) Park, N.; Sun, K.; Sun, Z. L.; Jing, Y.; Wang, D. L. High Efficiency NiO/ZnO Heterojunction UV Photodiode by Sol-Gel Processing. *J. Mater. Chem. C* **2013**, *1*, 7333−7338.

(12) Chen, X. M.; Ruan, K. B.; Wu, G. H.; Bao, D. H. Tuning Electrical Properties of Transparent p-NiO/n-MgZnO Heterojunctions with Band Gap Engineering of MgZnO. *Appl. Phys. Lett.* **2008**, *93*, 3.

(13) Bhattacharya, P.; Das, R. R.; Katiyar, R. S. Comparative Study of Mg Doped ZnO and Multilayer ZnO/MgO Thin Films. *Thin Solid Films* **2004**, *447*, 564−567.

(14) Bhattacharya, P.; Das, R. R.; Katiyar, R. S. Fabrication of Stable Wide-Band-Gap ZnO/MgO Multilayer Thin Films. *Appl. Phys. Lett.* **2003**, *83*, 2010−2012.

(15) Ohtomo, A.; Kawasaki, M.; Koida, T.; Masubuchi, K.; Koinuma, H.; Sakurai, Y.; Yoshida, Y.; Yasuda, T.; Segawa, Y. $Mg_xZn_{1-x}O$ as a II-VI Widegap Semiconductor Alloy. *Appl. Phys. Lett.* **1998**, *72*, 2466−2468.

(16) Sawai, Y.; Hazu, K.; Chichibu, S. F. Surface Stoichiometry and Activity Control for Atomically Smooth Low Dislocation Density ZnO and Pseudomorphic MgZnO Epitaxy on a Zn-Polar ZnO Substrate by the Helicon-Wave-Excited-Plasma Sputtering Epitaxy Method. *J. Appl. Phys.* **2010**, *108*, 063541.

DOI: 10.1021/acsami.5b01420
ACS Appl. Mater. Interfaces 2015, 7, 9660−9667

(17) Auret, F. D.; Goodman, S. A.; Hayes, M.; Legodi, M. J.; van Laarhoven, H. A.; Look, D. C. Electrical Characterization of 1.8 MeV Proton-Bombarded ZnO. *Appl. Phys. Lett.* **2001**, *79*, 3074−3076.
(18) Das, S.; Chakrabarti, S.; Chaudhuri, S. Optical Transmission and Photoluminescence Studies of ZnO-MgO Nanocomposite Thin Films. *J. Phys. D: Appl. Phys.* **2005**, *38*, 4021−4026.
(19) Yang, W.; Vispute, R. D.; Choopun, S.; Sharma, R. P.; Venkatesan, T.; Shen, H. Ultraviolet Photoconductive Detector Based on Epitaxial $Mg_{0.34}Zn_{0.66}O$ Thin Films. *Appl. Phys. Lett.* **2001**, *78*, 2787−2789.
(20) Endo, H.; Sugibuchi, M.; Takahashi, K.; Goto, S.; Hane, K.; Kashiwaba, Y. Fabrication and Characteristics of a Pt/$Mg_xZn_{1-x}O$ Schottky Photodiode on a ZnO Single Crystal. *Phys. Status Solidi C* **2008**, *5*, 3119−3121.
(21) Haruyuki, E.; Michiko, K.; Masahumi, A.; Yasuhiro, K.; Kazuhiro, H.; Yasube, K. High-Sensitivity Mid-Ultraviolet Pt/$Mg_{0.59}Zn_{0.41}O$ Schottky Photodiode on a ZnO Single Crystal Substrate. *Appl. Phys. Express* **2008**, *1*, 051201.
(22) Sharma, A. K.; Narayan, J.; Muth, J. F.; Teng, C. W.; Jin, C.; Kvit, A.; Kolbas, R. M.; Holland, O. W. Optical and Structural Properties of Epitaxial $Mg_xZn_{1-x}O$ Alloys. *Appl. Phys. Lett.* **1999**, *75*, 3327−3329.
(23) Choopun, S.; Vispute, R. D.; Yang, W.; Sharma, R. P.; Venkatesan, T.; Shen, H. Realization of Band Gap above 5.0 eV in Metastable Cubic-Phase $Mg_xZn_{1-x}O$ Alloy Films. *Appl. Phys. Lett.* **2002**, *80*, 1529−1531.
(24) Maruyama, T.; Arai, S. The Electrochromic Properties of Nickel Oxide Thin Films Prepared by Chemical Vapor Deposition. *Sol. Energy Mater. Sol. Cells* **1993**, *30*, 257−262.
(25) Takagi, T.; Tanaka, H.; Fujita, S.; Fujita, S. Molecular Beam Epitaxy of High Magnesium Content Single-Phase Wurzite $Mg_xZn_{1-x}O$ Alloys ($x \simeq 0.5$) and Their Application to Solar-Blind Region Photodetectors. *Jpn. J. Appl. Phys.* **2003**, *42*, L401.
(26) Ohtomo, A.; Kawasaki, M.; Sakurai, Y.; Ohkubo, I.; Shiroki, R.; Yoshida, Y.; Yasuda, T.; Segawa, Y.; Koinuma, H. Fabrication of Alloys and Superlattices Based on ZnO Towards Ultraviolet Laser. *Mater. Sci. Eng., B* **1998**, *56*, 263−266.
(27) Debnath, R.; Xie, T.; Wen, B.; Li, W.; Ha, J. Y.; Sullivan, N. F.; Nguyen, N. V.; Motayed, A. A Solution-Processed High-Efficiency p-NiO/n-ZnO Heterojunction Photodetector. *RSC Adv.* **2015**, *5*, 14646−14652.
(28) Liu, K. W.; Shen, D. Z.; Shan, C. X.; Zhang, J. Y.; Yao, B.; Zhao, D. X.; Lu, Y. M.; Fan, X. W. $Zn_{0.76}Mg_{0.24}O$ Homojunction Photodiode for Ultraviolet Detection. *Appl. Phys. Lett.* **2007**, *91*, 201106.
(29) Shukla, G. $Zn_{1-x}Mg_xO$ Homojunction-Based Ultraviolet Photodetector. *IEEE Photonics Technol. Lett.* **2009**, *21*, 887−889.
(30) Nguyen, N. V.; Sayan, S.; Levin, I.; Ehrstein, J. R.; Baumvol, I. J. R.; Driemeier, C.; Krug, C.; Wielunski, L.; Hung, P. Y.; Diebold, A. Optical Band Gaps and Composition Dependence of Hafnium−Aluminate Thin Films Grown by Atomic Layer Chemical Vapor Deposition. *J. Vac. Sci. Technol., A* **2005**, *23*, 1706−1713.
(31) Shannon, R. Revised Effective Ionic Radii and Systematic Studies of Interatomic Distances in Halides and Chalcogenides. *Acta Crystallogr., Sect. A: Cryst. Phys., Diffr., Theor. Gen. Crystallogr.* **1976**, *32*, 751−767.
(32) Sarver, J. F.; Katnack, F. L.; Hummel, F. A. Phase Equilibria and Manganese-Activated Fluorescence in the System $Zn_3(PO_4)_2$-$Mg_3(PO_4)_2$. *J. Electrochem. Soc.* **1959**, *106*, 960−963.
(33) Koike, K.; Hama, K.; Nakashima, I.; Takada, G.; Ogata, K.; Sasa, S.; Inoue, M.; Yano, M. Molecular Beam Epitaxial Growth of Wide Bandgap ZnMgO Alloy Films on (111)-Oriented Si Substrate toward UV-Detector Applications. *J. Cryst. Growth* **2005**, *278*, 288−292.
(34) Ghosh, R.; Basak, D. Composition Dependence of Electrical and Optical Properties in Sol-Gel $Mg_xZn_{1-x}O$ Thin Films. *J. Appl. Phys.* **2007**, *101*, 023507.
(35) Ghosh, R.; Basak, D. Optical Studies on $Mg_xZn_{1-x}O$ Wide Band Gap Semiconductor in the Perspective of Phase Equilibrium. *J. Mater. Sci.: Mater. Electron.* **2007**, *18*, 141−144.
(36) Singh, A.; Vij, A.; Kumar, D.; Khanna, P. K.; Kumar, M.; Gautam, S.; Chae, K. H. Investigation of Phase Segregation in Sol−Gel Derived ZnMgO Thin Films. *Semicond. Sci. Technol.* **2013**, *28*, 025004.
(37) Yin, Z.; Zheng, Q.; Chen, S.-C.; Cai, D.; Zhou, L.; Zhang, J. Bandgap Tunable $Zn_{1-x}Mg_xO$ Thin Films as Highly Transparent Cathode Buffer Layers for High-Performance Inverted Polymer Solar Cells. *Adv. Energy Mater.* **2014**, *4*, 1301404.
(38) Fujihara, S.; Sasaki, C.; Kimura, T. Effects of Li and Mg Doping on Microstructure and Properties of Sol-Gel ZnO Thin Films. *J. Eur. Ceram. Soc.* **2001**, *21*, 2109−2112.
(39) Hierro, A.; Tabares, G.; Ulloa, J. M.; Muñoz, E.; Nakamura, A.; Hayashi, T.; Temmyo, J. Carrier Compensation by Deep Levels in $Zn_{1-x}Mg_xO$/Sapphire. *Appl. Phys. Lett.* **2009**, *94*, 232101.
(40) Park, N.; Sun, K.; Sun, Z.; Jing, Y.; Wang, D. High Efficiency NiO/ZnO Heterojunction UV Photodiode by Sol-Gel Processing. *J. Mater. Chem. C* **2013**, *1*, 7333−7338.
(41) Ben Amor, M.; Boukhachem, A.; Boubaker, K.; Amlouk, M. Structural, Optical and Electrical Studies on Mg-Doped NiO Thin Films for Sensitivity Applications. *Mater. Sci. Semicond. Process.* **2014**, *27*, 994−1006.
(42) Ishida, Y.; Fujimori, A.; Ohta, H.; Hirano, M.; Hosono, H. Potential Profiling of the Nanometer-Scale Charge-Depletion Layer in n-ZnO/p-NiO Junction Using Photoemission Spectroscopy. *Appl. Phys. Lett.* **2006**, *89*, 153502.
(43) Soudi, A.; Dhakal, P.; Gu, Y. Diameter Dependence of the Minority Carrier Diffusion Length in Individual ZnO Nanowires. *Appl. Phys. Lett.* **2010**, *96*, 253115.
(44) Fan, M. M.; Liu, K. W.; Zhang, Z. Z.; Li, B. H.; Chen, X.; Zhao, D. X.; Shan, C. X.; Shen, D. Z. High-Performance Solar-Blind Ultraviolet Photodetector Based on Mixed-Phase ZnMgO Thin Film. *Appl. Phys. Lett.* **2014**, *105*, 011117.
(45) Hou, Y. N.; Mei, Z. X.; Liang, H. L.; Ye, D. Q.; Gu, C. Z.; Du, X. L. Dual-Band MgZnO Ultraviolet Photodetector Integrated with Si. *Appl. Phys. Lett.* **2013**, *102*, 153510.
(46) Zhao, Y.; Zhang, J.; Jiang, D.; Shan, C.; Zhang, Z.; Yao, B.; Zhao, D.; Shen, D. Ultraviolet Photodetector Based on a MgZnO Film Grown by Radio-frequency Magnetron Sputtering. *ACS Appl. Mater. Interfaces* **2009**, *1*, 2428−2430.
(47) Liu, K. W.; Zhang, J. Y.; Ma, J. G.; Jiang, D. Y.; Lu, Y. M.; Yao, B.; Li, B. H.; Zhao, D. X.; Zhang, Z. Z.; Shen, D. Z. $Zn_{0.8}Mg_{0.2}O$-based Metal−Semiconductor−Metal Photodiodes on Quartz for Visible-Blind Ultraviolet Detection. *J. Phys. D: Appl. Phys.* **2007**, *40*, 2765.
(48) Tabares, G.; Hierro, A.; Ulloa, J. M.; Guzman, A.; Muñoz, E.; Nakamura, A.; Hayashi, T.; Temmyo, J. High Responsivity and Internal Gain Mechanisms in Au-ZnMgO Schottky Photodiodes. *Appl. Phys. Lett.* **2010**, *96*, 101112.
(49) Kim, D. Y.; Ryu, J.; Manders, J.; Lee, J.; So, F. Air-Stable, Solution-Processed Oxide p-n Heterojunction Ultraviolet Photodetector. *ACS Appl. Mater. Interfaces* **2014**, *6*, 1370−1374.

DOI: 10.1021/acsami.5b01420
ACS Appl. Mater. Interfaces 2015, 7, 9660−9667